Compact implementation of Fourier transform two-dimensional IR spectroscopy without phase ambiguity

Jan Helbing* and Peter Hamm

Physikalisch-Chemisches Institut, Winterthurerstrasse 190, 8057 Zürich, Switzerland
**Corresponding author: j.helbing@pci.uzh.ch*

Received September 14, 2010; accepted November 4, 2010;
posted November 10, 2010 (Doc. ID 134915); published December 22, 2010

We describe an optimized setup for two-dimensional (2D) IR spectroscopy, which can be implemented at low additional cost and with standard optics in any laboratory equipped for femtosecond mid-IR spectroscopy. An interferometer produces a pair of intense pump pulses, whose interferogram is simultaneously recorded and directly yields the relative phase needed for the calculation of absorptive 2D spectra. We analyze different sampling methods based on a realistic noise model and introduce fast population time modulation as an alternative to the use of choppers in the suppression of scatter. Signal levels are compared to those of a photon-echo setup. © 2010 Optical Society of America

OCIS codes: 120.6200, 320.7150.

1. INTRODUCTION

During the past decade, two-dimensional (2D) spectroscopy has developed from a challenging experiment for specialized laser laboratories into a sensitive tool for the investigation of chemical, physical, and biological systems [1–11]. 2D-IR spectroscopy was initially devised as a narrow band pump–broadband probe experiment [12]. It is most versatile in a photon-echo configuration, with full intensity and polarization control over each individual field in the nonlinear mixing process [13,14]. Here, phase stability and precise knowledge of the relative phase of the laser fields at the sample is necessary to separate absorptive and dispersive signals and to achieve the highest possible spectral resolution and information content [15,16]. Since "phasing" and phase control are not required when recording the intrinsically absorptive 2D-IR spectra by the frequency-domain pump-probe method, this original version of 2D-IR involves much less experimental effort [17], and has thus remained attractive [18,19] despite its lower time and spectral resolution and lower sensitivity. The pump-probe experiment is also insensitive to phase shifts introduced by, for example, an additional laser beam that triggers a photoreaction. The recording of absorptive transient 2D-IR spectra is thus relatively straightforward in this experimental arrangement [20].

Many years ago, Wiersma *et al.* explored the close relationship between a heterodyne-detected photon echo and a Fourier transform (FT) pump-probe experiment with a collinear pair of pump pulses [1], and their formal analogy was analyzed by Faeder and Jonas [21]. Since then, it has been demonstrated both in the IR [22,23] and the visible [24,25] spectral range that the latter method can combine many advantages of the photon echo and the frequency domain 2D techniques. A collinear pump geometry has also been employed to record 2D THz spectra [26]. DeFlores *et al.* used a Mach–Zehnder interferometer to produce a mid-IR pump pulse pair and dispersed the second output of the interferometer to calibrate the time delay between them [22]. Zanni *et al.* generated the pulse pair with the help of a pulse shaper, which has the advantage that its relative phase is exactly known and can be varied at wish [27]. Here, we build on the interferometer method of Tokmakoff *et al.* [22], and present a compact setup that is much simpler than a pulse shaper, but still allows us to automatically phase the 2D-IR spectrum. A HeNe laser continuously tracks the delay changes between the pump pulses. The second mid-IR output of the interferometer is used to repeatedly record interferograms of the pump pulse pair, from which their relative phase is uniquely determined.

The scope of this paper is to present and discuss all necessary practical details for the construction and operation of what we believe is the most simple, yet fully functional FT 2D-IR experiment without phase ambiguity. This includes, of course, several concepts that have been previously described in the cited literature.

2. MOTIVATION

The main difference between a third-order photon-echo and a pump-probe experiment is the fact that the time ordering of the first and second field interactions is unknown in the former, while it is uniquely defined by the direction of the echo signal in the latter (see Fig. 1). This makes it possible to separately measure different Liouville space pathways. In particular, contributions arising from so-called "rephasing" diagrams, characterized by oscillations of opposite phase during the two coherence time periods, and "nonrephasing" diagrams (same oscillation phase during the two coherence times) can be distinguished. However, in order to obtain absorptive line shapes, which yield the highest spectral resolution, both contributions must be added [15]. In practice, the coherence time t_1 is thus scanned twice, with inverted time ordering of pulses 1 and 2, [see Fig. 1 left]. In a pump-probe geometry with a collinear pair of pump pulses, on the other hand, the same rephasing and nonrephasing signals are emitted simultaneously into the direction

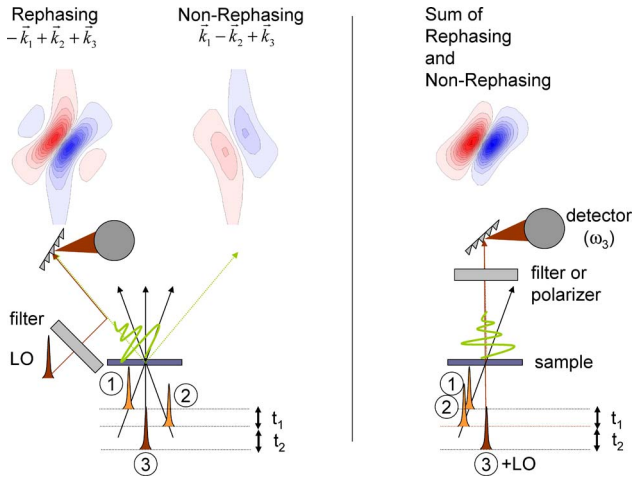

Fig. 1. (Color online) Schematic view of a FT 2D experiment in a (left) photon-echo geometry and a (right) pump-probe geometry. In the echo geometry, so-called rephasing and nonrephasing signals are emitted in different directions. They are recorded by the same detector after inverting the time order of pulses 1 and 2 and must be added to obtain purely absorptive 2D spectra. In the pump-probe geometry, pulses 1 and 2 are collinear, and the sum of rephasing and nonrephasing signals is measured directly.

of the probe beam, and t_1 needs to be scanned only once. Furthermore, the probe beam also acts as the local oscillator (LO), which interferes with the emitted third-order polarization for heterodyne detection, whereas a separate LO beam is needed in the echo geometry. This considerably reduces the experimental effort of 2D-IR spectroscopy to the optimization of a single overlap and the determination of the relative phase of two collinear mid-IR pump beams.

3. SETUP

In practice, the 2D experiment only requires the addition of an interferometer to a standard mid-IR pump-probe setup, as shown in Fig. 2(a). Tunable pulses (80–100 fs, 2 mJ) are generated by an optical parametric amplifier (OPA). Two reflections of a wedged CaF_2 window produce probe and reference beams (brown line in Fig. 2). Their diameter is enlarged by a factor of 1.5 in a telescope, and they are tightly focused (70 μm FWHM) onto different spots on the sample, dispersed in a monochromator, and detected by a double-array mercury-cadmium-telluride (MCT) detector with 32 pixels. The main fraction of the mid-IR light (orange lines in Fig. 2) enters a Mach–Zehnder interferometer (total footprint 16×16 cm^2). The beams in the two interferometer arms experience the same material dispersion (inside the beamsplitters BS1 and BS2) as well as two gold mirror reflections (M1, M2 and M3, M4). We use the interferometer output generated by a single beamsplitter reflection per beam in order to excite the sample. The two pump pulses thus have identical energies, independent of the exact beamsplitter reflectivity (nominally 50%). They are focused to a spot size of ≈100 μm FWHM in spatial overlap with the probe beam. The second interferometer output is collimated onto a pyroelectric detector (at room temperature) in order to record a linear pump pulse interferogram during every interferometer scan with the help of simple sample-and-hold electronics.

We do not collect data on a predefined grid of time points, but continuously move the interferometer arm during data acquisition and trace the delay changes with a HeNe laser beam.

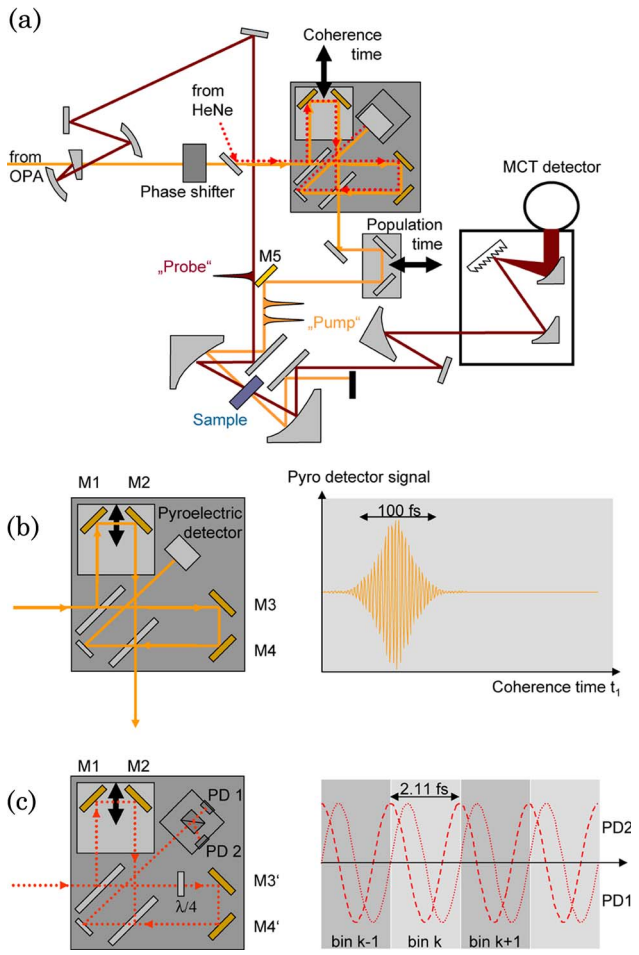

Fig. 2. (Color online) (a) Schematic representation of the setup. (b) Beam path of the mid-IR light in the interferometer. A pyroelectric detector records pump pulse interferograms during every coherence time scan. (c) Beam path for the HeNe laser propagating 2 cm above the mid-IR beam with separate beam splitters BS1′ and BS2′ and static mirrors M3′ and M4′ for independent alignment. Interference between a circular polarized beam ($\lambda/4$ plate in the static interferometer arm) and a linear polarized beam gives rise to two orthogonally polarized signals with a relative 90° phase shift used for quadrature fringe counting. Mid-IR beam splitters BS1 and BS2 may also be replaced by polarizers for measurements with perpendicular polarized pump pulses.

The HeNe beam propagates approximately 2 cm on top of the IR beam inside the interferometer (red dotted lines in Fig. 2). It is reflected by the same moving mirrors as the mid-IR beam (M1, M2), but we use separate beam splitters. Each pair of mid-IR and HeNe beam splitters is firmly fixed to the same mount, while a pair of adjustable gold mirrors for each beam (attached to a single base) in the static arm allows us to separately optimize mid-IR (M3, M4) and HeNe (M3′, M4′) overlap, without losing the necessary stability of the interferometer. For example, optimal overlap and interference of the mid-IR pump pulses is simply achieved by separately optimizing a pump-probe signal when blocking the static arm (and tuning the external mirror M5) and the moving arm (and tuning mirror M4) of the interferometer. Only slight readjustments are necessary even after realigning the OPA.

In order to establish an equidistant time grid, we count the number of fringes of the HeNe laser interferogram and sort the mid-IR data according to the fringe number (bin) at the instant of pulse emission. All data within a given time bin is averaged.

This is equivalent to a convolution of the time-domain signal with a narrow square window function or a multiplication of the frequency-domain signal by the corresponding FT, which is exactly known (a sinc function) and varies only slowly with wavelength in the mid-IR.

In the simplest form of measurement, the interferometer is scanned relatively slowly (e.g., 2 fs delay in 5–10 ms), corresponding to a few pulsed laser triggers per HeNe fringe. It is thus possible to record the HeNe laser interferogram with a single photodiode and digitize this signal at the same rate and with the same data acquisition card that is used for mid-IR data acquisition. Fringe counting can be done in the computer and yields a precise measure of the monotonous delay changes during a single t_1 scan. Since the absolute delay can be recovered for each individual scan from the simultaneously recorded interferogram of the mid-IR pump pulses (see Section 4), multiple forward and backward scans can be averaged.

Faster scans require a fringe counting scheme that is not limited by the repetition rate of the femtosecond laser or the relatively slow data acquisition card. In addition, bin numbers must be determined reproducibly, since the mid-IR interferogram of a single fast scan is no longer sufficient to correct for shifts. In this case, we use a standalone quadrature counting method based on [28,29]. A $\lambda/4$ wave plate is inserted into the HeNe beam in the static arm of the interferometer, producing circular polarization. The sum of the circular polarized beam and the linear polarized beam from the moving arm is split into two perpendicular polarized components by a polarization cube oriented at 45° relative to the incident polarization [see Fig. 2(c)]. The two signals have a relative phase difference of 90° and are used for continuous quadrature counting of the HeNe fringes at arbitrary speed and direction of delay changes. Only the fringe numbers at the instant of the femtosecond pulse emission are read by the computer synchronous with the mid-IR data, which is averaged in the corresponding time bin. A detailed scheme of the very compact counting and pyrodetector electronics is available from the authors and will be developed into a kit for interested laboratories.

For scanning the t_1 time, we use a small DC motor (PI M-111-1.DG) with rotary encoder, which is not precise enough to sample a sufficiently equidistant time grid. Both our fast and slow HeNe fringe counting schemes, however, allow for efficient, unbiased averaging of data in time bins of the duration of a HeNe oscillation period (2.11 fs), which eliminates any spectral artifact that may arise from imperfect motor motion. To ensure a uniform sampling of the time bins, we even add random delays to the motor starting position of each t_1 sweep. Much simpler linear motor stages should thus be equally suitable.

4. PHASE DETERMINATION AND SIGNAL PROCESSING

The absolute delay between the two pump pulses and their relative phase is determined to very high precision in a way similar to the method used in FTIR spectrometers.

Starting from an approximate time zero [a sampling point or time bin $\kappa = \kappa_0$ close to the maximum of the pump pulse interferogram $I(t_1)$ shown in Fig. 3(a)], a discrete FT yields a spectral amplitude and phase:

$$A(\omega_1[j]) = \sum_{\kappa=1}^{N} I(t_1[\kappa]) \exp\left(-2\pi i \frac{(\kappa-\kappa_0)(j-1)}{N}\right) = |A(\omega_1[j])| \exp(i\phi_{\kappa_0}(\omega_1[j])). \quad (1)$$

In order to perform this operation with automated fast FT routines, the first $\kappa_0 - 1$ points of the list $I(t_1[\kappa])$ have to be shifted to the end.

The slope of the phase $d\phi_{\kappa_0}/d\omega_1$ near the maximum of the spectrum is negative if κ_0 is chosen too small and positive if κ_0 is chosen too large [see the dotted curves for $\kappa_0 = 99$ and $\kappa_0 = 113$ in Fig. 3(b)]. This offers a precise way to find the sampling bin K closest to delay zero in an iterative search. K and the associated, spectrally flat phase factor ϕ_K, which is needed to compute the real part of the 2D spectrum can thus be determined automatically by the computer during data acquisition. For the data shown in Fig. 3, $K = 106$, and $\phi_K = -0.263$ is the offset of the corresponding, almost horizontal, solid curve in Fig. 3(b).

The MCT array detector measures the probe-beam intensity as a function of frequency ω_3, coherence time t_1, and waiting time t_2, which is a sum of several contributions [21,25]:

$$S(\omega_3, t_2, t_1) \propto |E_{\text{probe}}(\omega_3) + i\omega_3[P^{(1)}(\omega_3) + P^{(3)}_{\text{ppl}}(\omega_3, t_2) + P^{(3)}_{\text{pp2}}(\omega_3, t_2, t_1) + P^{(3)}_{2D}(\omega_3, t_2, t_1)] + E_{\text{scatter}}(\omega_3, t_2, t_1)|^2. \quad (2)$$

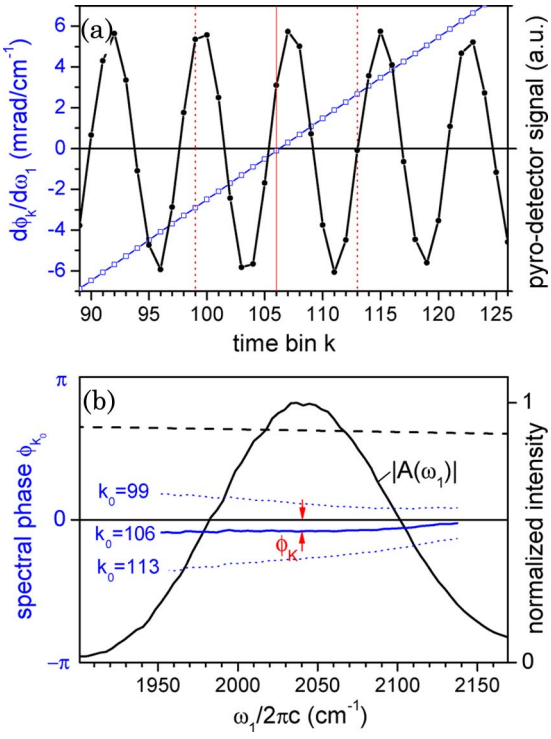

Fig. 3. (Color online) Phase determination: (a) central section of the pump pulse interferogram recorded by the pyroelectric detector (circles). Open squares show the slope of the spectral phase near the band center after FT of the interferogram starting at different time bins κ_0 (scale on left axis). (b) Spectrum $|A(\omega_1)|$ of the pump pulses (solid black curve) and flat spectral phase $\phi_K(\omega_1)$ (blue curve) obtained after FT of the interferogram with $\kappa_0 = K = 106$. Dotted curves show $\phi_{\kappa_0}(\omega_1)$ for $\kappa_0 = 99$ and $\kappa_0 = 113$. The black dashed curve in (b) indicates the weak intensity scaling caused by averaging data over one HeNe laser period.

The spectral density of the probe pulse and linear absorption (linear polarization $P^{(1)}(\omega_3)$) are normalized out by dividing by the reference signal. The pump-probe signal due to the third-order polarization generated by two field interactions with the same pump pulse ($P^{(3)}_{\mathrm{pp}}(\omega_3, t_2, t_1)$) are either static (pulse 1) or change only slowly (pulse 2) as a function of coherence time t_1 (they are not oscillatory) and are eliminated by Fourier transformation. In the absence of scattering, the absorptive 2D signal is thus directly obtained from the discrete FT:

$$S_{2D}(\omega_3, t_2, \omega_1[j]) = \mathrm{Re}\left[\Delta t \sum_{\kappa'=1}^{N'} \bar{S}(\omega_3, t_2, t_1[\kappa' + K - 1]) \times \exp\left(-2\pi i \frac{(\kappa' - 1)(j - 1)}{N'} - i\phi_K\right)\right], \quad (3)$$

where Δt is the width of the time bins and ϕ_K is the relative phase between the two pump pulses at $t_1 = t_1[K]$, determined from the pump pulse interferogram. $\bar{S}(\omega_3, t_2, t_1[\kappa])$ is the probe intensity of Eq. (2), recorded at the spectrometer frequency ω_3 in the time bin κ, divided by the corresponding intensity of the reference beam. This division greatly improves the signal-to-noise ratio and corrects for the finite width of the probe spectrum. Zero padding can be used to make $N' = N$ in Eq. (1) in order to obtain the same frequency grid.

The 2D signal calculated using Eq. (3) can also be automatically corrected for the effects of averaging the data in coherence time windows of one HeNe laser period, as well as for the finite width of the pump pulse spectrum: The binning of data in the time domain corresponds to a multiplication of the frequency domain spectra by the FT of a square of width $\Delta t = 2.11$ fs:

$$I_{\mathrm{bin}}(\omega_1) = \frac{\sin(\Delta t \omega_1)}{2\pi \Delta t \omega_1}. \quad (4)$$

This sinc function is shown as a dashed curve in Fig. 3(b). Furthermore, the response of the pyroelectric detector is practically wavelength independent, so the spectrum of the pump pulses at the sample is directly given by the amplitude of the FT of the mid-IR interferogram. As this is recorded on the same time grid as the actual data, it already contains the effect of data binning. A corrected 2D spectrum, corresponding to a measurement with infinitely broad pump and probe pulses is thus obtained by dividing Eq. (3) by $|A(\omega_1)|$. It is easily seen from Fig. 3(b) that data binning has a negligible effect compared to the limited spectral width of the pump pulses, which is often not corrected for in the literature.

Note that the imaginary part of the FT in Eq. (3) does not yield the dispersive part of the 2D-IR spectrum. In fact, the signal $\bar{S}(\omega_3, t_2, t_1)$ is in principle fully symmetric with respect to t_1, such that the imaginary part of its FT should vanish. However, we have to restrict the FT to positive coherence times because this symmetry is broken by the population time dependence of $\bar{S}(\omega_3, t_2, t_1)$. If the full complex 2D spectrum is desired, it must be computed from the absorptive spectrum via a pseudo-Kramers–Kronig transform, as outlined, for example, in [25].

5. PRACTICAL ASPECTS OF DATA COLLECTION

A. Fast Versus Slow Interferometer Scanning

The simplest form of operation of our setup, based on the simultaneous digitization of the HeNe laser photodiode and mid-IR signals, requires relatively slow changes of the coherence time (approximately 10 s for a t_1 scan of 3 ps). To normalize out slow intensity fluctuations, we then need to chop one or both of the pump pulses at half the laser repetition rate. To calculate the 2D signal, $\bar{S}$ in Eq. (3) is replaced by the ratio $\bar{S}_{\mathrm{pump\ on}}/\bar{S}_{\mathrm{pump\ off}}$. Taking the ratio instead of the difference corrects for different probe and reference beam intensities and the different response of individual detector elements. Without chopping, $\bar{S}(\omega_3, t_2, t_1[\kappa])$ should be divided by its average over all $t_1[\kappa]$ for the same reason.

Much higher scan speeds are possible when we use the independent quadrature counting scheme for delay tracking. It is then possible to fully exploit the relatively long-lived intensity correlation of the mid-IR pulses, which, in our system, decays with a time constant of approximately 60 ms (probe divided by reference intensity after gated integration and digitization). A scan speed corresponding to Nyquist sampling (four points per mid-IR optical cycle) thus yields a very high degree of correlation in the spectral window of interest, and a single t_1 scan of 3 ps at $\lambda = 5$ μm now only requires 0.4 s. However, to uniformly record data in all time bins, multiple scans are needed.

In Fig. 4, we compare, for the different scan modes, spectra computed from simulated interferograms, based on realistic motor motion (monotonic with random deviations from linear) and a realistic noise model, with an exponential intensity correlation decay of 60 laser triggers (see Appendix A for details). Each of the four signals corresponds to approximately 32,000 triggers. This data is collected in two back and forward scans over 6 ps at a slow scanning speed and 40 scans at a high scanning speed, equivalent to five to eight data points in total per time bin. The advantage of chopping in the slow scan mode [Figs. 4(a) and 4(b)] is clearly visible. Even more striking is the signal-to-noise enhancement when the scan speed is increased by a factor of 20 to approximate Nyquist sampling [Fig. 4(c) and 4(d)]. In the fast scans, however, the chopper is no longer useful, as it reduces the effective correlation between subsequent sampling points in addition to reducing the averaging statistics by a factor of 2.

B. Scattering Suppression

When a fraction β of the pump beams reaches the MCT detector because of scattering, the extra term in Eq. (2) gives rise to the additional signal

$$S_{\mathrm{scatter}}(\omega_3, t_2, t_1) \propto |E_{\mathrm{probe}}(\omega_3) + \beta[E_{\mathrm{pump1}}(\omega_3, t_2) + E_{\mathrm{pump2}}(\omega_3, t_2, t_1)]|^2. \quad (5)$$

The contribution due to E_{pump2} can be eliminated by chopping the static arm of the interferometer, while the interference between the static pump pulse 1 and the probe beam is eliminated by the t_1 FT [22]. When $|E_{\mathrm{probe}}| \gg \beta|E_{\mathrm{pump}}|$, the remaining term proportional to $\beta^2|E_{\mathrm{pump}}|^2$ can be neglected.

If no chopper is used in fast interferometer scans, an alternative strategy to suppress scattering background must be found. An elegant solution is to periodically invert the relative

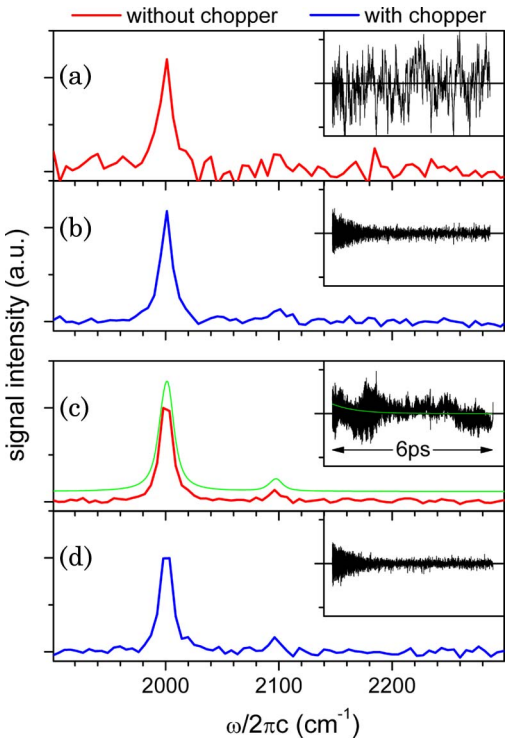

Fig. 4. (Color online) Effect of interferometer scan speed and chopping on signal to noise, illustrated by simulated Fourier spectra of two weak absorbers at 2000 and 2100 cm^{-1} (intensity ratio 10∶1). (a), (b) Slow t_1 motor motion (0.06 mm/s). (c), (d) Fast t_1 motor motion (1.25 mm/s). Blue [(b) and (d)] and red [(a) and (c)] curves represent Fourier transformed data with and without chopping, respectively. The insets in each graph show the simulated time domain data. The smooth curves in (c) indicate the analytic results.

phase between the pump pulses and the probe pulse. With a pulse shaper generating the pump pulses, a pure phase inversion is possible [27]. This changes only the sign of the scattering contribution, but not that of the desired third-order polarization. Scattering is thus eliminated by adding the two data sets. In the much simpler interferometer setup, a pseudo-phase inversion can be achieved by changing the population time t_2 by half a period of the mid-IR carrier frequency ω_0 [30]. However, adding data recorded for two population times $t_2 \pm \pi/(2\omega_0)$ fully eliminates only the scattering at the center frequency of the laser pulse. As shown in Appendix B, scattering suppression of more than 2 orders of magnitude over 10% bandwidth (e.g., a spectral window of 200 cm^{-1} at 5 μm) is nevertheless possible by adding data recorded at population times t_2 (with double weight) and $t_2 \pm \pi/\omega_0$. In our current setup, this is achieved by modulating the population time at one quarter of the laser repetition rate, using a photoelastic modulator to which the laser is synchronized [31] (phase shifter in Fig. 2(a)]. As a much simpler alternative, a librating Brewster window can be inserted into the pump or probe beam [32]. An illustration of the power of this method is shown in Fig. 5 for a strongly scattering sample.

C. Signal Size

The third-order polarization is proportional to the product of all three excitation fields. In an echo setup, these are ideally all equal so the echo intensity is proportional to $(\sqrt{I_0/3})^3$, where I_0 is the total available mid-IR intensity (after splitting off the weak LO beam). In the pump-probe geometry, the

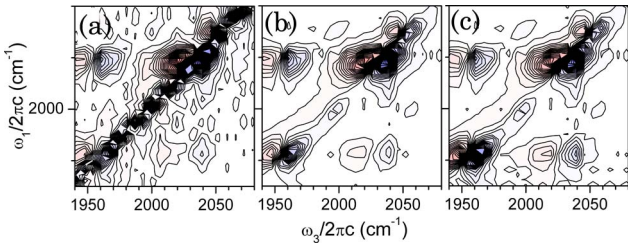

Fig. 5. (Color online) Absorptive 2D spectra at of the Osmium carbonyl complex Os(dcbpy) $I_2(CO)_2$ attached to the porous surface of a nanoporous TiO_2 film. Two sets of diagonal and cross peaks originate from two different binding configurations [34] (t_1 FT of the array detector signal with the phase factor ϕ_K automatically determined from the pump pulse interferogram, waiting time $t_2 = 1.5$ ps). (a) Data recorded without pseudo-phase modulation. (b) Same sample spot but with t_2 delay modulated at $f_{rep}/4$ between $t_2 \pm \pi/\omega_0$ to suppress scatter to second order. (c) Same data as in (b) after correction for the pump pulse spectrum.

third excitation field is provided by the probe pulse, and the corresponding polarization is proportional to $\sqrt{I_{probe}} \times \sqrt{I_{pump1} \times I_{pump2}}$. Like the LO in the echo setup, the probe beam is usually a small reflection of a CaF_2 or ZnSe window with an intensity $I_{probe} = \alpha I_0$. Using conventional 50% beam splitters, only half of the light entering the interferometer is directed onto the sample, so $I_{pump1} = I_{pump2} \approx I_0/4$. As a result the ratio of echo intensity and (pump-probe) polarization,

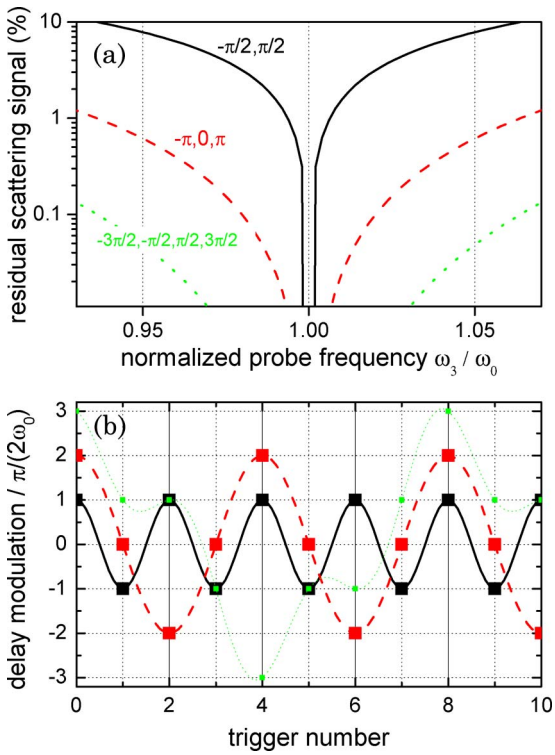

Fig. 6. (Color online) (a) Amplitude of the residual scattering signal $\cos^n(\pi\omega_3/\omega_0)$ (in percentage of the original) after summing over two (black solid curve, $n = 1$), three (red dashed curve, $n = 2$), or four (green dotted curve, $n = 3$) population delays in steps of π/ω_0. (b) Fast population time modulation, producing the correct amplitude and multiplicity of delays. Black solid curve, modulation amplitude $\pi/(2\omega_0)$, $f_{rep}/2$; red dashed curve, modulation amplitude $\pi/(2\omega_0)$, $f_{rep}/4$; green dotted curve, two modulators, amplitude ratio $(1+\sqrt{2})$∶1, frequencies $f_{rep}/8$ and $3f_{rep}/8$, relative phase shift $\pi/4$.

$$S_{\text{echo}}/S_{\text{pump-probe}} \approx \frac{1}{4\sqrt{\alpha}}\Big/\left(\frac{1}{\sqrt{3}}\right)^3 \approx \frac{0.77}{\sqrt{\alpha}}. \quad (6)$$

For a typical value of $\alpha = 0.04$ (CaF_2 window) the echo intensity is thus approximately four times larger than the corresponding polarization in the pump-probe geometry. Increasing α usually brings no improvement, since in the pump-probe geometry the LO is identical to the probe beam, and additional filters, which are then needed to prevent detector saturation, attenuate both the LO and the emitted polarization. In contrast, in the echo setup, the LO can be attenuated independently, without weakening the echo. Consequently, the heterodyned 2D-IR signal in the pump-probe geometry is weaker than that recorded in the echo geometry by another factor $\sqrt{10^{-\text{OD}}}$, where OD is the optical density of the filter(s) placed between the sample and the detector. Depending on the sample transmission, this factor typically lies between 3 and 10 (OD1–OD2) for our nitrogen-cooled MCT array detector with $\alpha = 0.04$.

This significant difference in sensitivity is partially compensated by the simultaneous collection of rephasing and nonrephasing signals. In addition, a higher optical density of the sample, which also leads to reabsorption of the third-order polarization, can lead to a larger signal increase in the pump-probe geometry, when it allows one to remove filters in front of the detector. Tighter focusing is also more straightforward in the self-heterodyning pump-probe method. Furthermore, as pointed out by Xiong and Zanni, polarization can be used to independently control the strength of all four fields even in the pump-probe geometry [33]. In the interferometer setup, an orthogonal polarization of the two pump pulses can be achieved by replacing the beam splitters by polarizers. The full incident intensity (minus a small leakage needed for recording the pump pulse interferogram) is then available for the excitation of the sample. A third polarizer is placed behind the sample and blocks most of the probe beam, but fully transmits the polarization that is polarized orthogonal to it. Thus, it is possible to work with the same beam intensities as in an echo experiment without the need for filters between the sample and the detector and to achieve the same signal size and sensitivity. Compared to a 2D spectrum recorded with all field polarizations parallel, the diagonal signals are smaller by a factor of 3, while the cross peaks are often enhanced.

6. CONCLUSION

The pump-probe geometry with two collinear pump pulses has led to greatly simplified FT 2D experiments, which require only two laser beams and knowledge of a single phase factor in order to obtain absorptive spectra. In the visible spectral range, pulse shapers, which can generate the pump pulse pairs with a well-defined phase difference, are already commercially available. In the mid-IR, however, a significant amount of expertise is still needed for their construction and operation, and light losses weigh heavier owing to weaker sources and signals. Here, we have shown that a much simpler interferometer, combined with delay tracking and the removal of the phase ambiguity, can perform similarly well. In particular, an interferometer is compatible with fast coherence time scanning and efficient scattering suppression, which are important strengths of active phase control in the pump-probe geometry. Broadband beam splitters allow for quick wavelength changes without significant realignment. When equipped with polarizing beam splitters (such as grid polarizers), the interferometer-based pump-probe experiment can, in principle, even achieve the same sensitivity as an optimized echo setup. However, we see the main advantages of the interferometer technique in its relatively simple implementation and easy use, which should help to make 2D-IR a much more widespread spectroscopic probe. The adaptation of the method for different frequency ranges, such as the far IR, may be equally promising.

Appendix A: Details of the Numeric Simulations

The parameters used in the simulations shown in Fig. 4 were chosen to mimic the performance of our setup. Each probe pulse intensity is normalized by the corresponding reference pulse, yielding a series of data points:

$$(I_{\text{probe}}/I_{\text{ref}})[i] = \text{const} + \text{sig}(t[i]) + a_{\text{noise}}\Delta I[i]. \quad (A1)$$

Normally distributed noise with a standard deviation of 1 and an exponential correlation decay $1/\kappa = 1/60$ (laser triggers) is generated with the help of the equation

$$\Delta I[i+1] = \Delta I[i](1-\kappa) + \kappa \times \text{Rnd}\left[\frac{2}{\sqrt{2\kappa}}\right], \quad (A2)$$

where $\text{Rnd}[\sigma]$ is a random number generator for a Gaussian distribution with standard deviation σ. Typical for our setup is $a_{\text{noise}} \approx 1.5 \times 10^{-3}$ and $\text{const} \approx 1$. The simulated signal in the time domain is the sum of two exponentially decaying fields (Lorentzian bands), with the large band slightly smaller than the noise:

$$\begin{aligned}\text{sig}(t[i]) = 10^{-3} \times \theta(t[i])(&\cos(\omega_1 t[i])e^{-t[i]/\tau_1} \\ &+ 0.1\cos(\omega_2 t[i])e^{-t[i]/\tau_2}).\end{aligned} \quad (A3)$$

Here, $\theta(t)$ is the unit step function. In Fig. 4, we have used $\tau_1 = 0.9$ ps, $\tau_2 = 1$ ps, $\omega_1/(2\pi c) = 2000$ cm^{-1}, and$\omega_2/(2\pi c) = 2100$ cm^{-1}.

The time points $t[i]$ result from the simulated monotonous motor motion with random position errors. Signals calculated at these exact time points that lie within one HeNe time bin are averaged. Similar to the real experiment, a binned interferogram of a Gaussian pulse with the same phase as the signal is computed at the simulated time points and used to compute the phase for the FT of the data. In the simulations with chopper, we set $\text{sig}(t[i]) = 0$ for all even i and divide by these (bin averaged) data points before Fourier transformation.

Appendix B: Scattering Suppression by Population Time Modulation

The main background in a 2D spectrum often arises from scattering, i.e., when a small amount of light of one or several pump pulses reaches the detector and interferes with the probe (or LO). In a pump-probe configuration, the scattering signal as a function of probe frequency ω_3 and delay t between pump and probe pulse is given by

$$\mathrm{sc}_0(\omega_3,t)=\frac{|E_{\mathrm{probe}}+E_{\mathrm{scatter}}|^2}{|E_{\mathrm{probe}}|^2}=1+\beta'^2+2\beta'\cos(t\omega_3+\psi), \tag{B1}$$

where $|E_{\mathrm{scatter}}|/|E_{\mathrm{probe}}|=\beta'<<1$ and ψ is the phase difference between the electric fields of the pump and probe pulse when their envelopes overlap exactly. (The scattering contribution left after t_1 FT is due to the moving arm of the interferometer, so $t=t_2+t_1$.) The time-independent term $1+\beta'^2$ is eliminated by the t_1 FT, but the time- and frequency-dependent term $2\beta'\cos(t\omega_3+\psi)$ can become very large; if only 0.1% of the pump light is scattered onto the detector, the scattering signal is of the same size as a 5 mOD absorption change (i.e., much larger than many 2D signals of interest).

The idea of population time modulation is to mimic, by a corresponding shift of t, a carrier envelope phase change from ψ to $\psi+\pi$. The latter is only possible with a pulse shaper and completely inverts the scattering signal at all probe frequencies without affecting the third-order polarization. At a selected probe frequency ω_0, the same is achieved by changing the population time form $t-\frac{\pi}{2\omega_0}$ to $t+\frac{\pi}{2\omega_0}$. After averaging over the signals recorded at these two time delays, we are left with a scattering contribution of

$$\begin{aligned}\mathrm{sc}_1(\omega_3,t)&=\frac{1}{2}\left[\mathrm{sc}_0\left(\omega_3,t-\frac{\pi}{2\omega_0}\right)+\mathrm{sc}_0\left(\omega_3,t+\frac{\pi}{2\omega_0}\right)\right]\\&=1+\beta'^2+2\beta'\cos(\omega_3t+\psi)\cos\left(\pi\frac{\omega_3}{\omega_0}\right).\end{aligned} \tag{B2}$$

We see that sc_1 and sc_0 are exactly of the same form, so we can generalize

$$\begin{aligned}\mathrm{sc}_n(\omega_3,t)&=\frac{1}{2}\left[\mathrm{sc}_{n-1}\left(\omega_3,t-\frac{\pi}{2\omega_0}\right)+\mathrm{sc}_{n-1}\left(\omega_3,t+\frac{\pi}{2\omega_0}\right)\right]\\&=1+\beta'^2+2\beta'\cos(\omega_3t+\psi)\cos^n\left(\pi\frac{\omega_3}{\omega_0}\right),\end{aligned} \tag{B3}$$

which means that scattering can, in principle, be suppressed to arbitrary order around a central frequency ω_0 by averaging data recorded at population times in steps of $\frac{\pi}{\omega_0}$. The appropriate weights are given by Pascal's triangle. First- ($n=1$) and second-order ($n=2$) averaging are the most useful, since they are compatible with fast delay modulation, as illustrated in Fig. 6(b). Photoelastic modulators or ZnSe plates driven to perform librations at Brewster angle can be used to induce such population time shifts at the kHz repetition rate f_{rep} of the laser. For higher-order modulation ($n>2$), a combination of at least two delay modulators at different frequency and amplitude would be necessary [e.g., green curve in Fig. 6(b)]. When needed, scattering suppression to third order is thus more easily achieved by combining second-order delay modulation with a slow delay change of π/ω_0. Slow delay dithering is already used in many laboratories for the reduction of scatter contributions to 2D-IR spectra. However, it is usually much less efficient than fast modulation due to phase drifts and insufficient delay motor precision.

It should be noted that neither delay modulation nor chopping of the static beam reduce the higher order contribution from interference of scattered light of one pump beam with that of the other. When this becomes significant, measurements should be carried out with perpendicular polarized pump pulses.

ACKNOWLEDGMENTS

We would like to thank S. Garrett-Roe and P. Donaldson for fruitful discussions.

REFERENCES

1. W. P. de Boeij, M. S. Pshenichnikov, and D. A. Wiersma, "Ultrafast solvation dynamics explored by femtosecond photon echo spectroscopies," Annu. Rev. Phys. Chem. **49**, 99–123 (1998).
2. S. Mukamel and R. M. Hochstrasser, "2D spectroscopy," Chem. Phys. 266, 135–136 (2001) and all articles in that issue.
3. D. M. Jonas, "Two-dimensional femtosecond spectroscopy," Annu. Rev. Phys. Chem. **54**, 425–463 (2003).
4. M. L. Cowan, B. D. Bruner, N. Huse, J. R. Dwyer, B. Chugh, E. T. J. Nibbering, T. Elsaesser, and R. J. D. Miller, "Ultrafast memory loss and energy redistribution in the hydrogen bond network of liquid H_2O," Nature **434**, 199–202 (2005).
5. T. Brixner, J. Stenger, H. M. Vaswani, M. Cho, R. E. Blankenship, and G. R. Fleming, "Two-dimensional spectroscopy of electronic couplings in photosynthesis," Nature **434**, 625–628 (2005).
6. R. M. Hochstrasser, "Two-dimensional spectroscopy at infrared and optical frequencies," Proc. Natl. Acad. Sci. U. S. A. **104**, 14190–14196 (2007).
7. J. Bredenbeck, J. Helbing, C. Kolano, and P. Hamm, "Ultrafast 2D-IR spectroscopy of transient species," Chem. Phys. Chem. **8**, 1747–1756 (2007).
8. J. Zheng, K. Kwak, and M. D. Fayer, "Ultrafast 2D IR vibrational echo spectroscopy," Acc. Chem. Res. **40**, 75–83 (2007).
9. Z. Ganim, H. S. Chung, A. W. Smith, L. P. DeFlores, K. C. Jones, and A. Tokmakoff, "Amide I two-dimensional infrared spectroscopy of proteins," Acc. Chem. Res. **41**, 432–441 (2008).
10. J. P. Ogilvie and K. J. Kubarych, "Multidimensional electronic and vibrational spectroscopy: an ultrafast probe of molecular relaxation and reaction dynamics," Adv. At. Mol. Opt. Phys. **57**, 249–321 (2009).
11. S. Mukamel, Y. Tanimura, and P. Hamm, "Coherent multidimensional optical spectroscopy," 42, 1207–1209 (2009) and all articles in that issue.
12. P. Hamm, M. Lim, and R. M. Hochstrasser, "Structure of the amide I band of peptides measured by femtosecond nonlinear-infrared spectroscopy," J. Phys. Chem. B **102**, 6123–6138 (1998).
13. M. T. Zanni, N.-H. Ge, Y. S. Kim, and R. M. Hochstrasser, "Two-dimensional IR spectroscopy can be designed to eliminate the diagonal peaks and expose only the crosspeaks needed for structure determination," Proc. Natl. Acad. Sci. U. S. A. **98**, 11265–11270 (2001).
14. M. Khalil, N. Demirdöven, and A. Tokmakoff, "Coherent 2D IR spectroscopy: molecular structure and dynamics in solution," J. Phys. Chem. A **107**, 5258–5279 (2003).
15. M. Khalil, N. Demirdröven, and A. Tokmakoff, "Obtaining absorptive line shapes in two-dimensional infrared vibrational correlation spectra," Phys. Rev. Lett. **90**, 047401 (2003).
16. E. H. G. Backus, S. Garrett-Roe, and P. Hamm, "Phasing problem of heterodyne-detected two-dimensional infrared spectroscopy," Opt. Lett. **33**, 2665–2667 (2008).
17. V. Cervetto, J. Helbing, J. Bredenbeck, and P. Hamm, "Double-resonance versus pulsed fourier transform 2D-IR spectroscopy: an experimental and theoretical comparison," J. Chem. Phys. **121**, 5935–5942 (2004).
18. J. F. Cahoon, K. R. Sawyer, J. P. Schlegel, and C. B. Harris, "Determining transition-state geometries in liquids using 2D-IR," Science **319**, 1820–1823 (2008).
19. P. Bodis, M. R. Panman, B. H. Bakker, A. Mateo-Alonso, M. Prato, W. J. Buma, A. M. Brouwer, E. R. Kay, D. A. Leigh, and S. Woutersen, "Two-dimensional vibrational spectroscopy of rotaxane-based molecular machines," Acc. Chem. Res. **42**, 1462–1469 (2009).

20. J. Bredenbeck, J. Helbing, and P. Hamm, "Transient 2D-IR spectroscopy exploring the polarization dependence," J. Chem. Phys. **121**, 5943–5957 (2004).
21. S. M. G. Faeder and D. M. Jonas, "Two-dimensional electronic correlation and relaxation spectra: theory and model calculations," J. Phys. Chem. A **103**, 10489–10505 (1999).
22. L. P. DeFlores, R. A. Nicodemus, and A. Tokmakoff, "Two-dimensional fourier transform spectroscopy in the pump–probe geometry," Opt. Lett. **32**, 2966–2968 (2007).
23. S. H. Shim, D. B. Strasfeld, E. C. Fulmer, and M. T. Zanni, "Femtosecond pulse shaping directly in the mid-IR using acousto-optic modulation," Opt. Lett. **31**, 838–840 (2006).
24. E. M. Grumstrup, S. H. Shim, M. A. Montgomery, N. H. Damrauer, and M. T. Zanni, "Facile collection of two-dimensional electronic spectra using femtosecond pulse-shaping technology," Opt. Express **15**, 16681–16689 (2007).
25. J. A. Myers, K. L. Lewis, P. F. Tekavec, and J. P. Ogilvie, "Two-color two-dimensional Fourier transform electronic spectroscopy with a pulse-shaper," Opt. Express **16**, 17420–17428 (2008).
26. W. Kuehn, K. Reimann, M. Woerner, and T. Elsaesser, "Phase-resolved two-dimensional spectroscopy based on collinear *n*-wave mixing in the ultrafast time domain," J. Chem. Phys. **130**, 164503 (2009).
27. S.-H. Shim, D. B. Strasfeld, Y. L. Ling, and M. T. Zanni, "Multidimensional ultrafast spectroscopy special feature: automated 2D IR spectroscopy using a mid-IR pulse shaper and application of this technology to the human islet amyloid polypeptide," Proc. Natl. Acad. Sci. U. S. A. **104**, 14197–14202 (2007).
28. M. J. Downs and K. W. Raine, "An unmodulated bi-directional fringe-counting interferometer system for measuring displacement," Precis. Eng. **1**, 85–88 (1979).
29. L. Lepetit, G. Chériaux, and M. Joffre, "Linear techniques of phase measurement by femtosecond spectral interferometry for applications in spectroscopy," J. Opt. Soc. Am. B **12**, 2467–2474 (1995).
30. A. W. Albrecht, J. D. Hybl, S. M. G. Faeder, and D. M. Jonas, "Experimental distinction between phase shifts and time delays: implications for femtosecond spectroscopy and coherent control of chemical reactions," J. Chem. Phys. **111**, 10934–10956 (1999).
31. M. Bonmarin and J. Helbing, "Polarization control of ultrashort mid-IR laser pulses for transient vibrational circular dichroism measurements," Chirality : the pharmacological, biological, and chemical consequences of molecular asymmetry **21**, E298–E306 (2009).
32. R. Bloem, S. Garrett-Roe, H. Strzalka, P. Hamm, and P. Donaldson, "Enhancing signal detection and completely eliminating scattering using quasi-phase-cycling in 2D IR experiments," Opt. Express, **18**, 27067–27078 (2010).
33. W. Xiong and M. T. Zanni, "Signal enhancement and background cancellation in collinear two-dimensional spectroscopies," Opt. Lett. **33**, 1371–1373 (2008).
34. J. Korppi-Tommola, J. Helbing, N. Humalamäki, M. Haukka, E. Andresen, and P. Hamm, "Sensitizer exchange dynamics in air and solvent filled semiconductor nanocavities," in *International Conference on Ultrafast Phenomena*, OSA Technical Digest (CD) (Optical Society of America, 2010), paper ME15.